International Journal of Heat and Mass Transfer 145 (2019) 118752

Contents lists available at ScienceDirect

International Journal of Heat and Mass Transfer

journal homepage: www.elsevier.com/locate/ijhmt

Analytical and numerical predictions of the thermal performance of multi-layered lattice structures

Jean Ernot [a], Patrick G. Verdin [a,*], Hayder Ahmad [b], Philip Indge [b]

[a] Centre for Thermal Energy Systems and Materials, Cranfield University, Bedfordshire MK43 0AL, UK
[b] SAFRAN Electrical & Power UK LTD, Pitstone, Buckinghamshire LU7 9GT, UK

ARTICLE INFO

Article history:
Received 19 February 2019
Received in revised form 7 August 2019
Accepted 17 September 2019

Keywords:
Multi-layered lattice structures
Analytical model
Forced convection
CFD
Total heat dissipation

ABSTRACT

The recent development of additive manufacturing has allowed complex geometries such as multi-layered lattice structures to be designed for different applications, including heat transfer. Performing Computational Fluid Dynamics (CFD) analyses on each new design iteration of lattice structures would require high computational time and cost. An analytical model has therefore been developed, able to rapidly and cost-effectively predict the heat transfer of complex lattice structures. The numerical code has been written for a given multi-layered lattice sample and a two-step approach with fin analogy has been applied to determine the mean outlet fluid temperature and the total heat dissipation for air as the working fluid. CFD simulations have also been performed and results compared to the analytical ones. A very good agreement is obtained between numerical and analytical results under the defined industrial operating conditions of the complex lattice structures, showing that such analytical model can be quickly and efficiently applied to evaluate the thermal performance of multi-layered lattice structures.

1. Introduction

Heat removal is of significant relevance for most engineering applications involving mechanical and electronic components generating heat when operating. Heat sinks are usually employed to dissipate the heat generated by a system through fluid medium and to maintain the structure temperature at an acceptable level. Due to its simplicity to obtain and implement, air is the most commonly used cooling fluid [1]. In order to maximise the heat dissipation to coolant, various heat sinks geometries have been proposed over the last two decades and their thermal performance widely investigated: multiple types of fins (folded, brazed, pin) [2] and parallel plates [3], which are referred to as conventional designs [4], two-dimensional metallic honeycombs [5–9], metal foams [10,11] and lattice-frame materials (LFMs) [12] among others. Natural convection in conventional designs such as rectangular enclosures has been studied for some time. The conjugate heat transfer via natural convection and conduction in a triangular enclosure filled with a porous medium has been investigated in [13] where flow patterns, temperature and heat transfer have been analysed for different dimensionless thickness of the bottom wall, different thermal conductivity ratio between the solid material and the fluid, and Rayleigh numbers. It has been found that both thermal conductivity ratio and thickness of the bottom wall can be used as control parameters for the heat transport and the flow field. The entropy generation due to the conjugate natural convection heat transfer in a thick wall enclosure filled with a fluid-saturated porous medium has been numerically studied by the same authors in [14]. The authors considered an inclined right wall and obtained results for different Rayleigh numbers, wall thickness and inclination of the right wall, and thermal conductivity ratio. The influence of the position of a circular tube filled with air in a differentially heated cavity has been investigated in [15], showing that the tube position can lead to different flow fields and heat transfer intensities, which are also affected by the value of the Rayleigh number. A 2D Computational Fluid Dynamics (CFD) model has been considered in [16] to study the conjugate laminar mixed convection and conduction in a lid-driven enclosure with a thick bottom wall. It has been found that the heat transfer is a decreasing function of the Richardson number and thermal conductivity ratio, and a decreasing function of the wall thickness. It has also been established that the wall thickness is an effective parameter for higher thermal conductivity ratio and that the values of local and mean Nusselt numbers are close to each other for higher values of thermal conductivity ratio. A 2D CFD model has also been used in [17] to study the influence of solid and porous fins attached

* Corresponding author.
E-mail address: p.verdin@cranfield.ac.uk (P.G. Verdin).

https://doi.org/10.1016/j.ijheatmasstransfer.2019.118752
0017-9310/

Nomenclature

Dimensionless numbers

C_1, C_2	constants (Zukauskas, 1987) [–]
m, n	constants (Zukauskas, 1987) [–]
N	number of nodes in vertical direction [–]
Nu	Nusselt number [–]
Pr	Prandtl number [–]
Re	Reynolds number [–]

Greek letters

α	struts angle with respect to horizontal [°]
η	local coordinate along strut axis [m]
λ	constant from gov. equations for thermal fields [1/m]
λ_2	constant from gov. equations for thermal fields [1/m]
μ	dynamic viscosity of air [kg/m·s]
ν	kinematic viscosity of air [m^2/s]
ϕ_{bot_w}	rate of heat transfer from bottom wall to fluid [W]
ϕ_{lat}	rate of heat transfer from lattice to fluid [W]
ϕ_{si_w}	rate of heat transfer from side wall to fluid [W]
ϕ_{top_w}	rate of heat transfer from top wall to fluid [W]
ρ_f	fluid density [kg/m^3]
θ_0	defined as T_w - T_f [K]
θ_{si_w}	defined as T_{si_w} - T_f [K]
θ_{strut}	defined as T_{strut} - T_f [K]
ξ	local coordinate along wall axis [m]

Roman letters

$\dot{m}_{cell}$	mass flow rate entering a cell [kg/s]
$\dot{m}$	total mass flow rate [kg/s]
$\overline{h}$	overall heat transfer coefficient $[W/m^2.K]$
a	unit cell size [m]
C_p	specific heat of air [J/kg·K]
d	strut diameter [m]
H	height of the sample [m]
h_∞	local heat transfer coefficient $[W/m^2.K]$
k	thermal conductivity [W/m·K]
L	length of the sample [m]
l	strut length [m]
L_c	characteristic length [m]
L_{strut}	total strut length [m]
P_{si_w}	side wall perimeter [m]
P_{strut}	strut perimeter [m]
Q	total heat dissipation [W]
q	heat flux [W/m^2]
S	cross-sectional area of the heat sink [m^2]
$S_{c\_bot\_w}$	surf. area of bottom wall in contact with fluid [m^2]
$S_{c\_si\_w}$	surf. of vertical side wall in contact with top wall [m^2]
$S_{c\_st\_f}$	surf. area of struts in contact with fluid for convective heat transfer [m^2]
$S_{c\_top\_w}$	surf. area of top wall in contact with fluid [m^2]
S_{sample}	cross-sectional surf. area of sample [m^2]
S_{si_w}	cross sectional area of slice of side wall [m^2]
S_{strut}	cross-sectional surf. area of cylindrical struts for conductive heat transfer [m^2]
t	vertical side walls and top horizontal wall thickness [m]
T_0	inlet airflow temperature [K]
T_f	fluid temperature [K]
T_{bot_w}	bottom horizontal wall temperature [K]
T_{si_w}	vertical side wall temperature [K]
T_{strut}	strut temperature [K]
T_{top_w}	top horizontal wall temperature [K]
T_w	heating temperature [K]
u_0	inlet airflow velocity [m/s]
W	width of the sample [m]
x, y, z	global Cartesian coordinates [m]

Subscripts

d	diameter
f	fluid
in	inlet
lat	lattice
m	mean
max	maximum
out	outlet
s	solid
si	side
w	wall

to the hot wall of a differentiated heated inclined rectangular enclosure. The authors have investigated the average Nusselt number for different parameters including Rayleigh number, Darcy number, relative thermal conductivity ratio of solid phase to fluid, cavity inclination angle and aspect ratio, fin number, position, and length. The usage of fin techniques for heat transfer enhancement have been discussed in [18,19], for phase change material (PCM)-based heat storage, and in [20–23] for the thermal management of electronic devices. The unsteady laminar natural convection in a deferentially heated oblique cavity with flexible oscillating fin mounted on the bottom adiabatic wall has been investigated in [24] and detailed results have been shown for a wide range of non-dimensional time and Young modulus, thermal conductivity ratio, oscillation amplitude, left wall heater length and inclination angle of the wall. Natural convection has been investigated for water solidification problems, such as in [25] for studies performed with the open source CFD code OpenFOAM.

The recent development and increasing availability of additive manufacturing has allowed new and complex geometries to be conceived, such as multi-layered lattice structures, which present multiple advantages: light weight, high stiffness and large surface area to volume ratio. These structures are increasingly used in the aerospace industry for heat removal applications, particularly for aircraft electric motors, resulting in weight loss and cost saving. Performing CFD simulations for each design iteration of multi-layered lattice structures is not a practical solution as it has significant time and cost implications. To overcome such limitations, an analytical model able to predict the heat transfer efficiency of multi-layered lattice structures is proposed to allow for rapid and cost effective thermal analyses. Approximate analytical solutions based on a fin analogy are commonly considered for complex geometry heat sinks subject to forced convection [6,10–12]. Both fluid flow and heat transfer analyses would be extremely complex to solve using Navier-Stokes and energy equations [12]. A fin analysis is therefore generally employed to obtain the solid temperature distribution within the heat sink and obtain a consistent approximate solution of the physical problem. CFD-based results have been generated and compared to the analytical-based solutions; this has allowed to determine the accuracy and limits of the analytical model.

2. Numerical models

2.1. Analytical model

The thermal performance of complex geometry heat sinks is generally assessed with the total heat dissipation Q [6,10–12,26], also known as the total heat transfer rate, and is calculated as:

$$Q = \dot{m} C_p \left(T_{f,m,out} - T_{f,m,in}\right) \quad (1)$$

where $\dot{m}$ is the mass flow rate entering the heat sink, C_p is the specific heat of the fluid, $T_{f,m,out}$ is the mean outlet fluid temperature and $T_{f,m,in}$ is the mean inlet fluid temperature. The mass flow rate $\dot{m}$ entering the heat sink is given by:

$$\dot{m} = \rho_f u_0 S \quad (2)$$

where ρ_f is the fluid density, u_0 is the inlet airflow velocity and S is the cross-sectional area of the heat sink.

To calculate the total heat dissipation Q, the mean outlet fluid temperature has been determined analytically with MATLAB® R2015a. A two-step approach, presented in Sections 2.1.1 and 2.1.2, has been applied to solve for the studied physical problem.

The analytical model has been developed for the multi-layered lattice sample presented in Fig. 1a. This sample has been obtained by 3D-printing and is made of Aluminium with a typical thermal conductivity $k_s = 200\,\mathrm{W/m \cdot K}$ [6]. The studied sample is comprised of walls forming a channel which is filled by a lattice. The lattice part is defined as a set of body-centered cubic (BCC) unit cells, each composed of eight cylindrical struts of diameter $d = 0.002$ m and length $l = 0.0173$ m. A schematic diagram of the physical problem to be solved is shown in Fig. 1b, presenting the coordinates system considered and the overall dimensions of the heat sink. The heat sink is exposed to heating from the bottom surface where a uniform temperature T_w is applied, whilst the top and side surfaces are considered to be thermally insulated. Air is chosen as the cooling fluid and is forced to flow across the channel with an inlet temperature T_0 and an inlet velocity u_0. Radiation has been shown to be negligible when dealing with heat sinks thermal applications [5,6,8,10,12]. Therefore, only conductive and convective heat transfer mechanisms are considered when deriving the governing equations for thermal fields. Steady-state conditions were considered and thermal and physical properties of fluid and solid were assumed to be constant, according to previous published studies [6,11].

2.1.1. First step: solid temperature distribution

The first step of the analytical model consists in obtaining the temperature distribution within the solid parts composing the sample under forced convection.

2.1.1.1. Lattice. A fin analysis has been performed to determine the lattice temperature distribution along the sample height direction. As the heat transfer mechanism is assumed to be identical for all cylindrical struts composing the lattice part, only one set of struts along the height direction is studied. The lattice temperature distribution is assumed to vary only in the height direction. Due to the short length of the sample and the heating source uniformly applied on the bottom surface, the temperature variation with respect to the length and width directions can be neglected. The local coordinate η along the total strut length L_{strut} is considered when establishing the governing equation. A thermal balance is performed initially on an infinitesimal element experiencing convective and conductive heat transfer, as shown in Fig. 2. The governing equation for the strut temperature can be written as:

$$\frac{d^2 T_{strut}(\eta)}{d\eta^2} - \frac{h_\infty P_{strut}}{k_s S_{strut}} \left(T_{strut}(\eta) - T_f\right) = 0 \quad (3)$$

For the sake of simplicity, Eq. (3) has been rearranged considering $\theta_{strut} = T_{strut} - T_f$ and $\lambda^2 = \frac{h_\infty P_{strut}}{k_s S_{strut}}$, leading to the following final governing equation:

$$\frac{d^2 \theta_{strut}}{d\eta^2} - \lambda^2 \theta_{strut} = 0 \quad (4)$$

Eq. (4) can be solved subject to the following boundary conditions:

$$\begin{cases} \theta_{strut}(\eta = 0) = \theta_0 = T_w - T_f \\ k_s \frac{d\theta_{strut}}{d\eta}(\eta = L_{strut}) = 0 \end{cases} \quad (5)$$

At $\eta = 0$, a Dirichlet boundary condition is considered, with the temperature of the struts assumed equal to the external temperature applied on the heat sink bottom surface. As the bottom wall thickness is small (2 mm) and the material has a large thermal conductivity ($k_s = 200\,\mathrm{W/m \cdot K}$), heat loss within the bottom wall is neglected. At $\eta = L_{strut}$, a Neumann boundary condition is used,

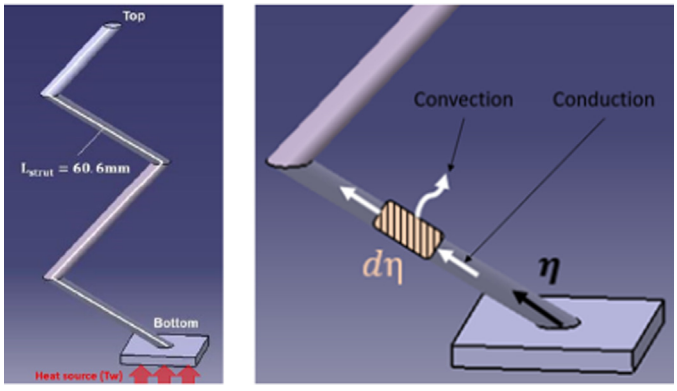

Fig. 2. Study of an infinitesimal element along the strut length.

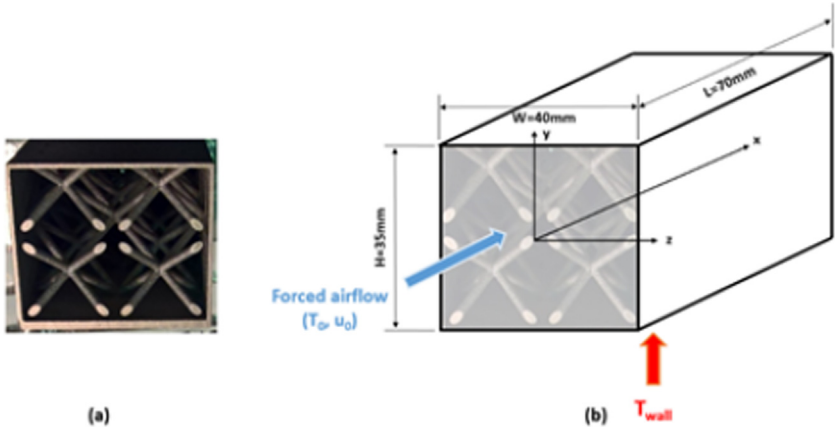

Fig. 1. Multi-layered lattice sample: Studied sample (a), Schematic diagram of the problem (b).

and for the sake of simplicity, the heat transfer at the end of the struts is assumed negligible. As mentioned in Section 2.1, the sample is considered thermally insulated on the top surface, i.e. considering no heat transfer with the outside domain. This top surface is assumed to have a uniform wall temperature defined by considering a weighted average temperature from the end of the struts and from the vertical side walls (method presented in Section 2.1.1.3). This represents an alternative approach, used to determine the top wall temperature and, therefore, the heat exchanged between the top wall and the fluid. This method is discussed and verified in Section 4.1.2.

The strut temperature distribution is obtained through Eqs. (6) and (7) for eight nodes along the height direction, as shown in Fig. 3. This discretisation will be further explained in Section 2.1.2 for the calculation of the fluid temperature.

$$\theta_{strut}(\eta) = \theta_0[\cosh(\lambda\eta) - \sinh(\lambda\eta)\tanh(\lambda L_{strut})] \tag{6}$$

$$T_{strut}(\eta) = T_f + \theta_{strut}(\eta) \tag{7}$$

with $\theta_0 = T_w - T_f$ and $L_{strut} = 0.061$ m is the cumulative length of all struts along the height direction.

2.1.1.2. Vertical side walls. The temperature distribution of the vertical side walls along the height direction is obtained with the same fin analysis as performed for the lattice. Due to the symmetry of the geometry with respect to the *x*-*y* plane, only one vertical side wall is considered, and more particularly one unit slice of the side wall along the length direction. The temperature distribution is assumed to be the same as for the entire side wall. A thermal balance is performed on an infinitesimal element along the side wall and a local axis ξ is used. Following the same steps as for the lattice part, and taking into account Eqs. (3)–(5), the temperature distribution of the vertical side wall can be obtained with:

$$\theta_{si\_w}(\xi) = \theta_0[\cosh(\lambda_2\xi) - \sinh(\lambda_2\xi)\tanh(\lambda_2 H)] \tag{8}$$

$$T_{si\_w}(\xi) = T_f + \theta_{si\_w}(\xi) \tag{9}$$

where $\lambda_2 = \sqrt{\frac{h_\infty P_{si\_w}}{k_s S_{si\_w}}}$ is the constant from the governing equation, $S_{si\_w} = ta$ is the cross-sectional area of the studied slice of side wall and $P_{si\_w} = a$, is the perimeter of the studied slice of side wall.

2.1.1.3. Top and bottom horizontal walls. The bottom horizontal wall temperature is assumed to be constant and equal to T_w applied to the heat sink, due to the large thermal conductivity of the wall material and its small thickness.

For the sake of simplicity, the temperature of the top wall is assumed to be uniform and is calculated, based on the temperature contribution from both the lattice and the vertical side walls, at the top of the sample. Fig. 4 shows the surface of the lattice and vertical side walls in contact with the top horizontal wall. Considering $L = 0.07$ m, $t = 0.001$ m and $d = 0.002$ m, the surface areas of the side wall and lattice in contact with the top wall appears to count for 62% and 38% of the total contact surface area, respectively. Therefore, the top horizontal wall temperature can be obtained by considering the weighted temperature from the lattice and the side wall at the top of the sample, as shown in Eq. (10).

$$T_{top\_w} = 0.38T_{strut}\left(y = \frac{H}{2}\right) + 0.62T_{si\_w}\left(y = \frac{H}{2}\right) \tag{10}$$

2.1.2. Second step: fluid temperature distribution

Based on the solid temperature distribution, the second step of the analytical model consists in calculating the fluid temperature variation across the sample. Therefore, the sample is discretised into layers and slices along the height and length directions respectively, as shown in Fig. 5, leading to multiple cells within the channel.

When air (of density $\rho = 1.2$ kg/m^3, kinematic viscosity $\mu = 1.8e-05$ kg/ms and thermal conductivity $k_f = 0.026$ W/m/K) flows through the heat sink, the temperature differences between the fluid and the solid parts, i.e. the lattice, side walls, top and bottom walls, induce some heat transfer which increases the fluid temperature along the sample. In order to model this fluid temperature variation, an energy balance, given by Eq. (11), is applied to each cell within the sample.

$$\dot{m}_{cell}C_p(T_{f,out} - T_{f,in}) = \phi_{lat} + \phi_{si\_w} \tag{11}$$

where $\dot{m}_{cell}$, is the mass flow rate entering each cell, $T_{f,out}$ and $T_{f,in}$ are the fluid temperature at the outlet and at the inlet of each cell respectively, C_p is the specific heat of air and ϕ_{lat} and ϕ_{si_w} are the convective heat transfer rates from the lattice and side wall to the fluid given by Eqs. (12) and (13).

$$\phi_{lat} = h_{\infty_{lat}}S_{c\_st\_f}(T_{strut} - T_{f,in}) \tag{12}$$

$$\phi_{si\_w} = h_{\infty_{si\_w}}S_{c\_si\_w\_f}(T_{si\_w} - T_{f,in}) \tag{13}$$

where $S_{c\_st\_f} = 8P_{strut}l$, $S_{c\_si\_w\_f} = 2(a/2a)$, and h_∞ is the local heat transfer coefficient. Both strut and side wall temperatures within each cell are assumed constant and equal to the nodes temperatures in the middle of the cell. For the cells within Layers 1 and 4, shown in Fig. 5a, the heat contribution from bottom and top horizontal walls is added to the energy balance, considering ϕ_{bot_w} and ϕ_{top_w} defined by Eqs. (14) and (15), respectively:

$$\phi_{bot\_w} = h_{\infty_{bot\_w}}S_{c\_bot\_w\_f}(T_{bot\_w} - T_{f,in}) \tag{14}$$

$$\phi_{top\_w} = h_{\infty_{top\_w}}S_{c\_top\_w\_f}(T_{top\_w} - T_{f,in}) \tag{15}$$

with $S_{c\_top\_w\_f} = S_{c\_bot\_w\_f} = Wa$ and $T_{bot\_w} = T_w$.

The global mass flow rate $\dot{m}$ entering the heat sink, given by Eq. (2), is assumed constant along the heat sink due to its short

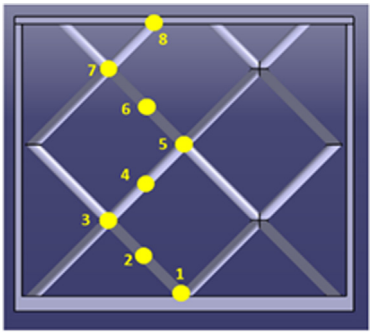

Fig. 3. Discretisation of one strut path into nodes.

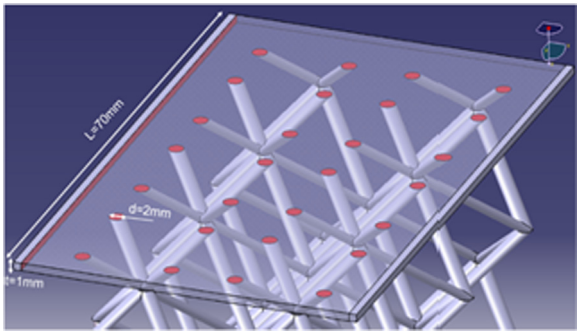

Fig. 4. Contact surfaces with top wall.

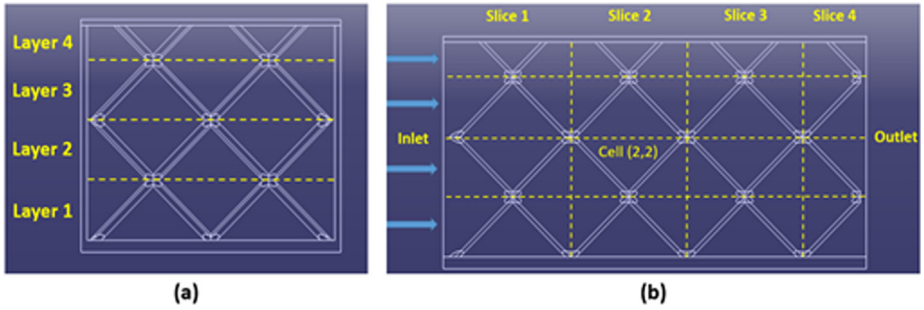

Fig. 5. Sample discretisation into layers, slices and cells: (a) front view, (b) side view.

length. Regarding Eq. (11), the mass flow rate entering each cell, $\dot{m}_{cell}$, is determined as a percentage of the global mass flow rate. The percentages considered for each cell are calculated, based on the ratio of the layer height ($a/2$ for Layers 1 to 3, $a/4$ for Layer 4, with $a = 20$ mm) over the sample height ($H = 35$ mm), giving 28.6% and 14.2% of the global mass flow rate for Layers 1 to 3 and Layer 4, respectively. Furthermore, it is assumed that no fluid mixing is present between the cells, suggesting that the heat contribution from both bottom and top walls only affects Layers 1 and 4. This implies that each layer is thermally insulated and that the fluid temperature at the inlet of a cell is equal to the outlet fluid temperature of the cell from the previous slice, and within the same layer.

2.1.3. Local heat transfer coefficient h_∞

Evaluating the local heat transfer coefficient h_∞ is required to solve for the heat transfer problem. A geometry analogy with tube-bank arrangements is considered for the multi-layered lattice sample, as performed in [12] with lattice-frame materials. Extensive experiments have been carried out on a forced flow around tube-bank arrangements, more particularly for both in-line and staggered arrays of cylinders [27]. The multi-layered lattice geometry is assumed to be equivalent to an in-line arrangement and the empirical correlations used for the calculation of h_∞ are provided by Eq. (16). For the studied sample, the constant C_1 is considered equal to 0.96 as the sample is assumed to have 7 tube rows along the flow direction. Furthermore, according to [27], a correction factor equal to $\sin(\alpha)^{0.6}$ can be applied to the empirical correlations to account for the struts inclination with respect to the horizontal plane. The angle α is found to be 35.3°, which leads to a value of the correction factor around 0.72.

$$h_{\infty_{lat}} = \begin{cases} C_1 \sin(\alpha)^{0.6} 0.9 Re_{d,max}^{0.4} Pr^{0.36} \frac{k_f}{d} & 0 < Re_d < 10^2 \\ C_1 \sin(\alpha)^{0.6} 0.52 Re_{d,max}^{0.5} Pr^{0.36} \frac{k_f}{d} & 10^2 < Re_d < 10^3 \\ C_1 \sin(\alpha)^{0.6} 0.27 Re_{d,max}^{0.63} Pr^{0.36} \frac{k_f}{d} & 10^3 < Re_d < 2.010^5 \end{cases} \quad (16)$$

The empirically calculated coefficient h_∞ concerns the heat transfer at the surface of the cylindrical struts. Regarding the vertical side walls and the horizontal walls, the local heat transfer coefficients are assumed equal to half the coefficient $h_{\infty_{lat}}$. This assumption is further discussed in Section 4.

2.2. CFD model

A CFD model is built to check the fluid temperature predicted analytically. The mesh is generated with ANSYS meshing, using tetrahedral elements, and exported into the commercial flow solver ANSYS Fluent® 18.2. As described previously, the physical problem involves a conjugate heat transfer within the sample, i.e. both conductive and convective heat transfers through solids and between fluid and solids, respectively. To account for this conjugate heat transfer, the 3D geometry of the studied sample is created with the Computer-Aided Design (CAD) software CATIA® V5-6R2013 and both fluid and solid domains are modelled, as described in Fig. 6. The overall dimensions of the sample are used for the 3D modelling and the same lattice geometry, as described previously, produced for the CFD analysis, i.e. with the same number and size of cylinders within the channel. Geometry simplifications are adopted for the interface between the lattice and the vertical side walls as no connections are considered. Note that the same simplifications have been assumed in the analytical model, as the temperature distributions of both the lattice and the vertical side walls are derived separately, and obtained without considering the heat interaction at these locations.

Conditions are applied at the boundaries of the computational domain. A velocity-inlet boundary condition is selected with a temperature T_0 and a flow velocity u_0. A gauge pressure of 0 Pa is applied at the pressure-outlet boundary condition. A thermal boundary condition with a heat flux of 0 W/m²·K is applied on the outer surfaces of the sample to model adiabatic conditions, and a constant temperature T_w is applied on the bottom surface of the model. Both no-slip wall and thermal *Coupled* conditions are considered for the fluid-solid interfaces. A *Coupled* thermal boundary condition is applied on the solid-solid interfaces, to model the conductive heat transfer mechanism through solids. Input values for T_0, u_0 and T_w are selected within the following ranges: $[284.8; 304.8]$ K, $[5.4; 11.0]$ m/s and $[300; 420]$ K, respectively. These values have been defined as representative of the industrial operating conditions for the final application of the complex lattice structures. For the sake of brevity, governing equations of the fluid flow and heat transfer are not provided here, but they can be retrieved from the Fluent User's Guide [28].

A pressure-based solver and steady-state conditions are selected, with both *Viscous-Laminar* and *Energy* models, to account for the simultaneous fluid flow and heat transfer analysis. The *SIMPLEC* scheme is used for the pressure-velocity coupling, and *PRESTO!* for the pressure. The convergence criteria for the velocity and energy equations are set to 5.10^{-4} and 10^{-6}, respectively.

A mesh-sensitivity analysis is performed, based on three meshes comprising 514,980, 644,672 and 900,553 nodes. Same input conditions, $T_0 = 294.82$ K, $u_0 = 9.1$ m/s and $T_w = 320$ K are considered for all 3 cases. Temperature and velocity distributions are plotted along two vertical lines located at mid-length and at the outlet of the sample, see Fig. 7. The solution from each mesh is seen to be grid independent and very little difference appears when comparing results. Although the coarse mesh (514,980 nodes) could have been used for the study, the medium mesh of 644,672 nodes has been preferred as it matches better the fine grid result next to the wall, and very little difference in computing time is needed when running this case compared to the coarser-based one.

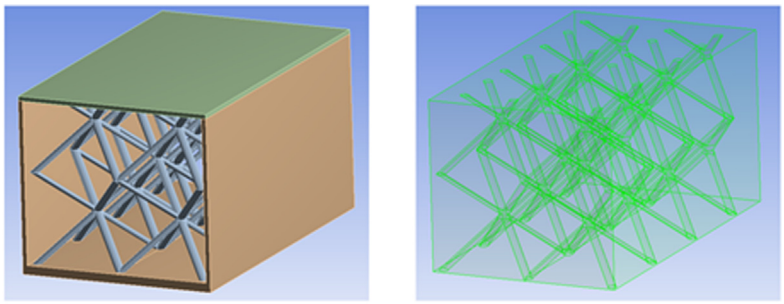

Fig. 6. Computational domain: (a) Solid, (b) fluid.

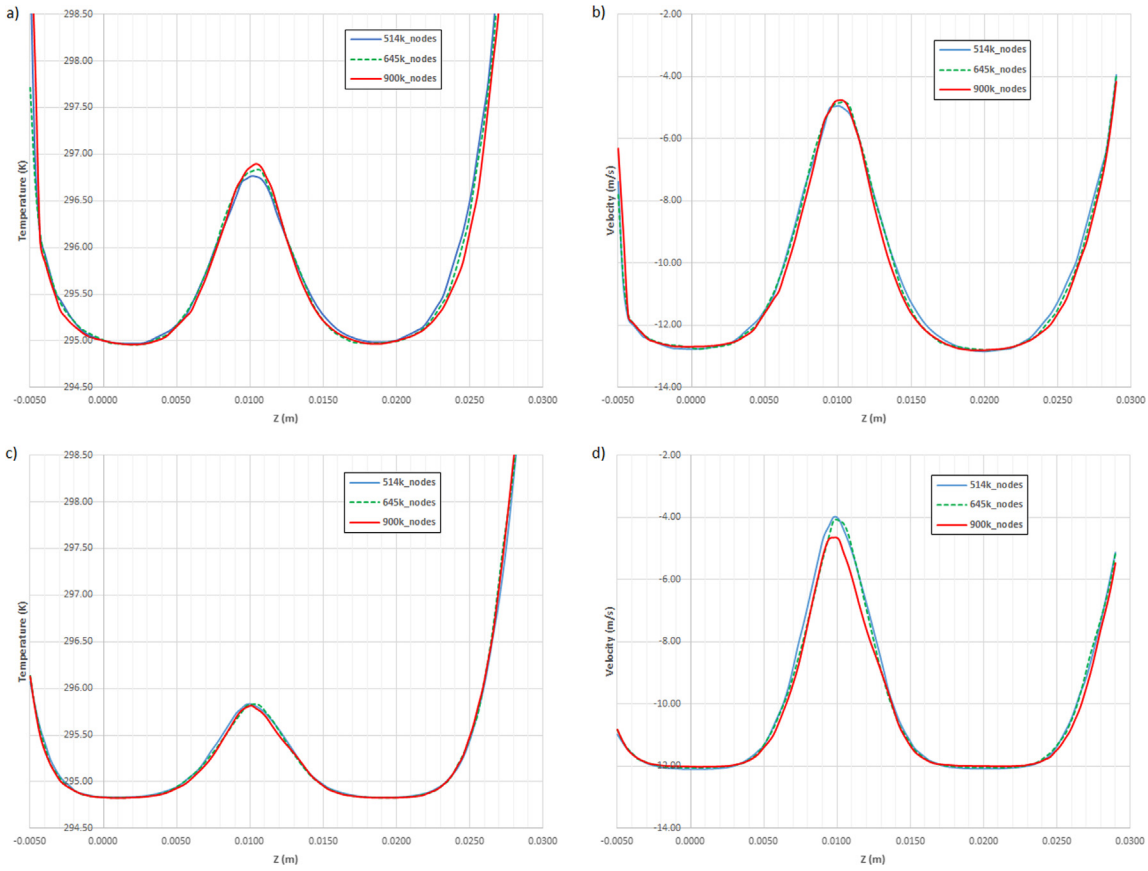

Fig. 7. (a) Temperature profile at the outlet, (b) velocity profile at the outlet, (c) temperature profile at sample mid-length, (d) velocity profile at sample mid-length.

3. Numerical results

3.1. Mean fluid temperature

The analytical fluid temperature distribution is determined for each cell within the sample, i.e. along the height and length directions. In order to verify the analytical predictions, the weighted average fluid temperature is calculated for each Plane j located at the end of the Slices j along the x-axis, with $j = \{1, 2, 3, 4\}$, as described in Fig. 8a. The fluid temperature distribution across each Plane j is given by the fluid temperature at the outlet of Cells (i, j), with $i = \{1, 2, 3, 4\}$ defining the height direction, as shown in Fig. 8b.

The mean fluid temperature of each plane is determined by considering the weighted temperature of each of the four cells, according to their surface with respect to the total surface area of the plane. Layer 4, on the top of the sample, represents only 14.2% of the total surface area of each plane, whereas, layers 1 to 3 represent the remaining 85.8%, with 28.6% per layer. These coefficients are applied when determining the weighted fluid temperature of each plane, as described by Eq. (17).

$$T_{f,plane\ j} = 0.286 * \left(T_{f,cell(1,j)} + T_{f,cell(2,j)} + T_{f,cell(3,j)}\right) + 0.142 * T_{f,cell(4,j)} \quad (17)$$

To allow comparison with the analytical mean fluid temperatures, four planes are created in the CFD model at the same locations, as shown in Fig. 9.

Analytical and numerical predictions of the mean fluid temperature at each plane are shown in Fig. 10. For the specific input conditions mentioned, a very good agreement is obtained between analytical and CFD mean fluid temperatures, especially at the out-

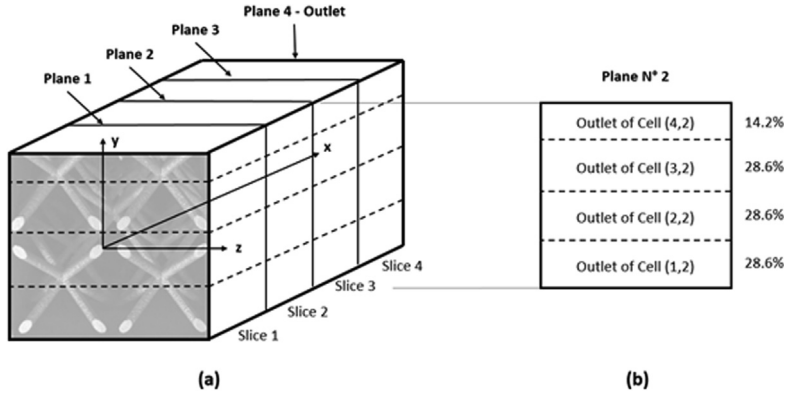

Fig. 8. Schematic diagram: (a) plane locations, (b) cells per plane and percentages of cells surface within the plane.

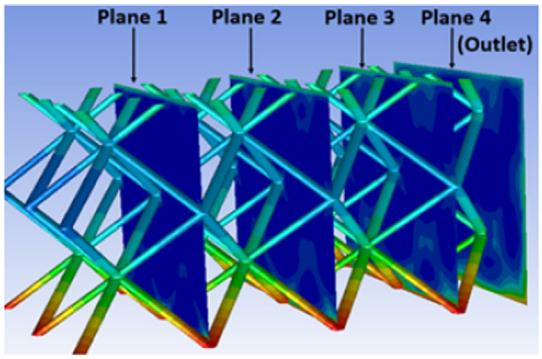

Fig. 9. Planes for mean fluid temperature calculations.

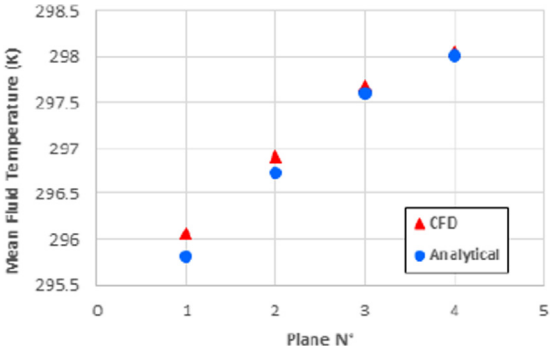

Fig. 10. Comparison of analytical and numerical means fluid temperatures for $T_0 = 294.82$ K, $u_0 = 9.1$ m/s and $T_w = 330$ K.

let (Plane n°4). However, to investigate the range of validity of the analytical model, a sensitivity analysis is performed on all three model inputs: heating temperature T_w, inlet airflow velocity u_0 and inlet airflow temperature T_0. Three sets of multiple simulations are carried out with variations of these inputs values.

The first set of simulations consists in studying the heating temperature applied on the bottom surface of the sample by considering a temperature rise from 300 to 420 K with an increment of 30 K between each simulation, keeping constant $u_0 = 9.1$ m/s and $T_0 = 294.8$ K. The second set of simulations consists in varying the inlet velocity from 5.4 to 11 m/s, with T_w and T_0 fixed at 320 K and 294.8 K, respectively. Finally, for the third set of simulations, the inlet airflow temperature varies from 284.8 to 304.8 K with an increment of 5 K between each simulation, keeping T_w at 350 K and u_0 at 9.1 m/s. As mentioned previously, these ranges of inputs values are selected to be in line with the industrial operating conditions of the final lattice structure.

Fig. 11 shows the variation of the average temperatures with respect to the heating temperature T_w applied on the sample at each plane. Both analytical and CFD predictions generally show a good match, even if a greater fluid temperature difference can be identified for the highest heating temperatures, i.e. when T_w is higher than 360 K, for Planes 1 and 2. The maximum relative errors between analytical and numerical average fluid temperatures are however very low, around 0.3%, 0.2%, 0.1% and 0.1% for Planes 1 to 4, respectively. This demonstrates that the analytical model works very well and is verified for the range of heating temperatures considered in this study: [300; 420] K.

Fig. 12 shows the analytical and numerical results obtained when varying the inlet velocity u_0, keeping constant $T_w = 320$ K and $T_0 = 294.8$ K. A very good agreement is obtained between analytical and CFD predictions for inlet velocities greater than 8 m/s. When looking at the plot, it seems that the analytical code fails to predict the correct mean temperature at low inlet velocities. However, the maximum error obtained when $u_0 = 5.4$ m/s is not larger than 0.3% when compared to the CFD results, showing that the analytical model also works well at low velocity.

The variations of the inlet airflow temperature on the average core temperature at the outlet are presented in Fig. 13. Both analytical and numerical predictions values are nearly identical, proving once again that the analytical model works well under the conditions considered in this work. In addition, both analytical and numerical results show a linear trends, this is consistent with previous results displayed in Fig. 11.

3.2. Total heat dissipation

The mean fluid temperature at the outlet is of particular interest compared to those obtained on other planes as it is used for the calculation of the total heat dissipation Q. Five simulations are performed, considering random values for T_w, u_0 and T_0 within the following respective ranges of values: [300; 420] K, [8.3; 11] m/s and [284.8; 304.8] K, as indicated in Table 1.

Analytical and numerical mean outlet fluid temperatures are derived for each simulation. Using Eqs. (1) and (2), with the sample cross-sectional area $S_{sample} = HW$, the fluid density $\rho_f = 1.2$ kg/m^3, the specific heat of air $C_p = 1000$ J/kg · K, and the values of u_0 and T_0 listed in Table 1, the values of the total heat dissipation Q have been calculated. The corresponding results are presented in Fig. 14. On average, the relative error between the analytical and the numerical total heat dissipation reaches 5.6%, which shows that a very good agreement is obtained between the two models for any random values within the designated ranges.

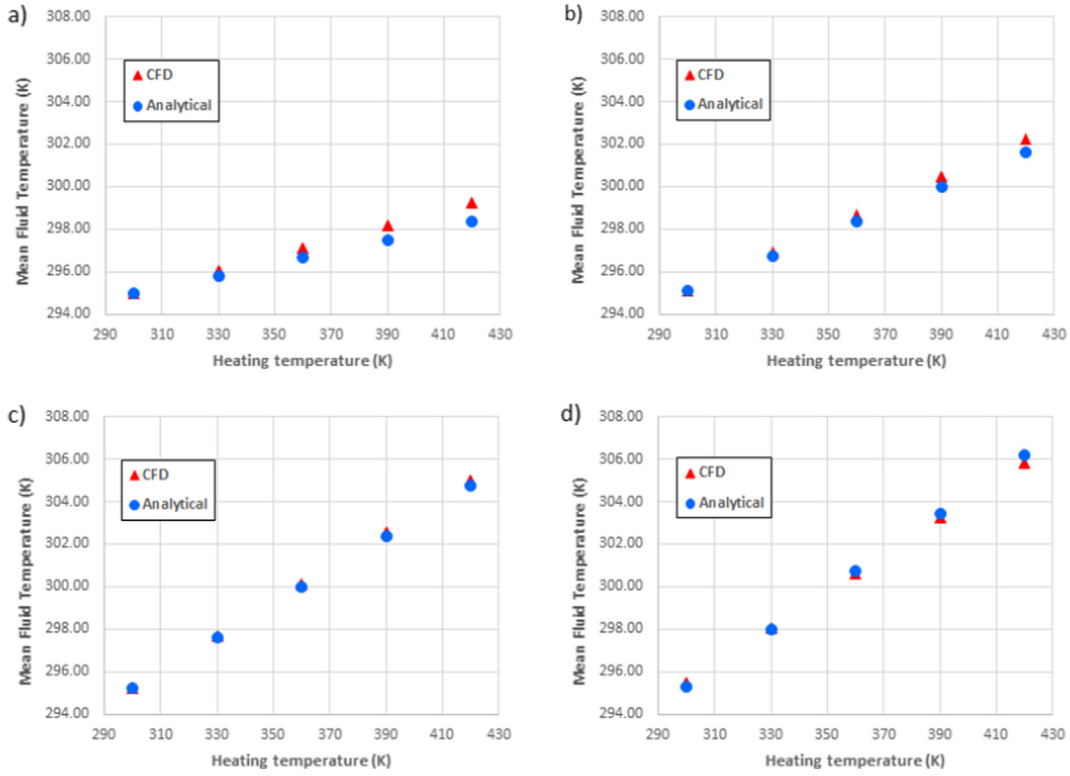

Fig. 11. Comparison between analytical and numerical mean fluid temperatures of Planes n° 1 (a), 2 (b), 3 (c) and 4 (d) with respect to T_w for $T_0 = 294.8$ K and $u_0 = 9.1$ m/s.

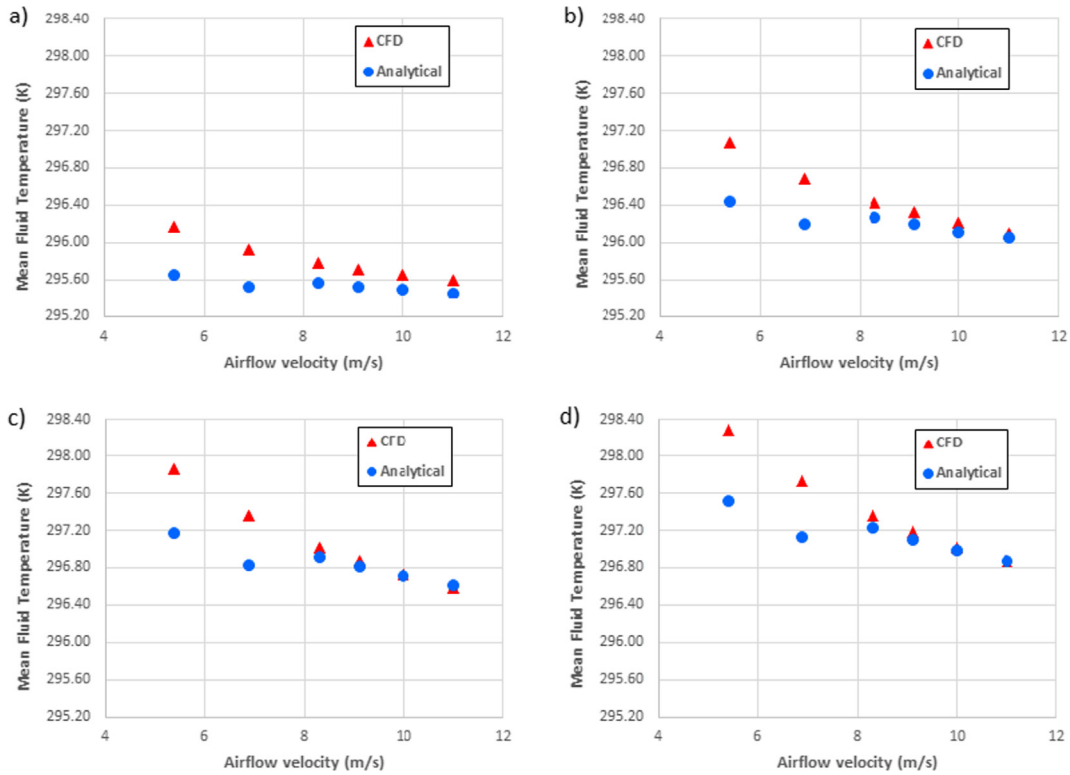

Fig. 12. Comparison between analytical and numerical mean fluid temperatures of Planes n° 1 (a), 2 (b), 3 (c) and 4 (d) with respect to u_0 for $T_w = 320$ K and $T_0 = 294.8$ K.

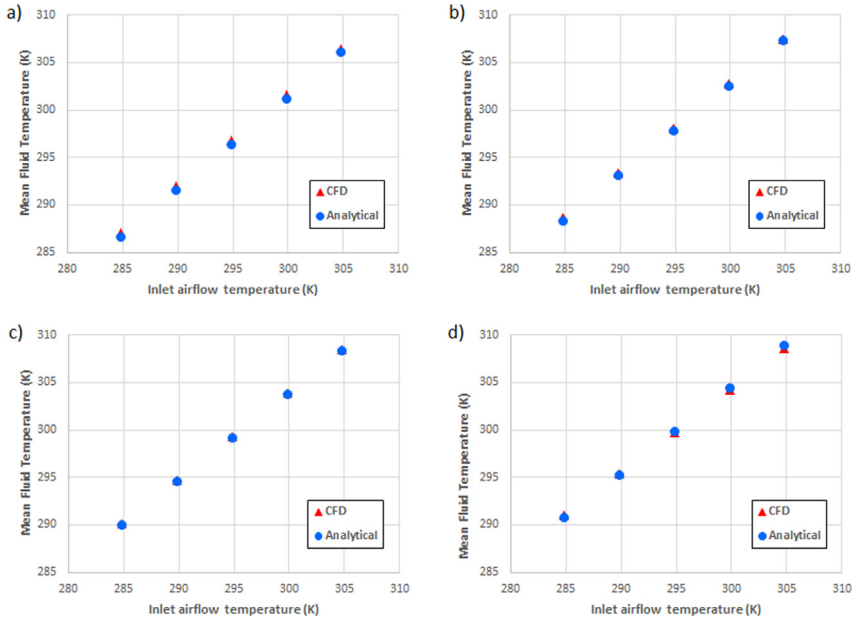

Fig. 13. Comparison between analytical and numerical mean fluid temperatures of Planes n° 1 (a), 2 (b), 3 (c) and 4 (d) with respect to T_0 for $T_w = 350$ K and $u_0 = 9.1$ m/s.

Table 1
Input values considered for the random simulations.

N° simulation	Random values		
	T_w [K]	u_0 [m/s]	T_0 [K]
1	383	9	299
2	345	11	302
3	419	10	289
4	322	9	298
5	347	11	297

4. Discussion

As shown in the previous section, the analytical model generally shows a good agreement with the CFD model. Different aspects related to the analytical model are discussed in the following sections, including the assumptions considered and the limits of the model.

4.1. Verification of assumptions

Assumptions have been considered when building the analytical model, for instance, for the calculation of the top wall temperature and for the local heat transfer coefficient at the walls.

4.1.1. Top wall temperature

Initially, the top wall temperature is assumed uniform and is calculated based on the lattice and the vertical side walls temperatures at the top of the sample, and with respect to their contact surfaces with this top wall, 38% and 62% of the total contact surface area, respectively. The temperature appears to vary slightly, reaching a 10 K difference, from the boundaries to the wall mid-width, as shown in Fig. 15. The average CFD-based top wall temperature has also been determined and little temperature difference is found between numerical and analytical top wall temperatures. The maximum difference reaches 3.2 K for the ranges of inputs considered. This implies that the assumptions used to analytically determine the top wall temperature are valid.

4.1.2. Local heat transfer coefficient

The local heat transfer coefficients of the lattice part, the vertical side walls and the bottom and top horizontal walls are numerically examined. The local heat transfer coefficient of the lattice, $h_{\infty_{lat}}$, has been set as a constant across the sample, considering the empirical correlations of forced flow around tube-bank arrangements, described in [27], and provided by Eq. (16). Regarding the vertical side walls, bottom, and top walls, the corresponding local heat transfer coefficients $h_{\infty_{si\_w}}, h_{\infty_{bot\_w}}$ and $h_{\infty_{top\_w}}$ are assumed equal to half the local heat transfer coefficient of the lattice $h_{\infty_{lat}}$. To check this assumption, the "surface heat transfer coefficient" of the solid domain has been calculated in Fluent. Fig. 16 shows the values of the local heat transfer coefficient across the heat sink under the specific inputs values: $u_0 = 9.1$ m/s, $T_0 = 294.8$ K, $T_w = 350$ K.

The local heat transfer coefficient of the lattice part is seen to vary at the surface of the cylinders, contrary to the empirically-derived coefficient. It can be observed from Fig. 16 that the value of the coefficient slightly decreases at the back of the cylinders, suggesting a lower heat transfer. Besides, the lattice part exhibits higher values of local heat transfer coefficient than estimated at the walls.

The average surface heat transfer coefficients of each solid part are also investigated for various inputs. The assumption of the local heat transfer coefficient being equal to half $h_{\infty_{lat}}$ seems valid in general, especially at T_w around 350 K. This ratio value of 1/2 still represents a fair approximation when the heating temperature is set close to the boundaries of the T_w range, i.e. at 310 K and 419 K.

As previously noticed, the analytical average fluid temperatures on Planes 1 and 2 are under-estimated compared to the CFD-based results. This difference may be explained by the numerical value of $h_{\infty_{lat}}$ which is seen to be much higher at the front of the sample. Therefore, a higher heat transfer is present for the CFD model than for the analytical model in the first two slices.

4.2. Limits for the airflow velocity

In general, a very good agreement between analytical and CFD predictions of the mean outlet fluid temperature and the total heat dissipation is obtained for the following ranges of inputs values:

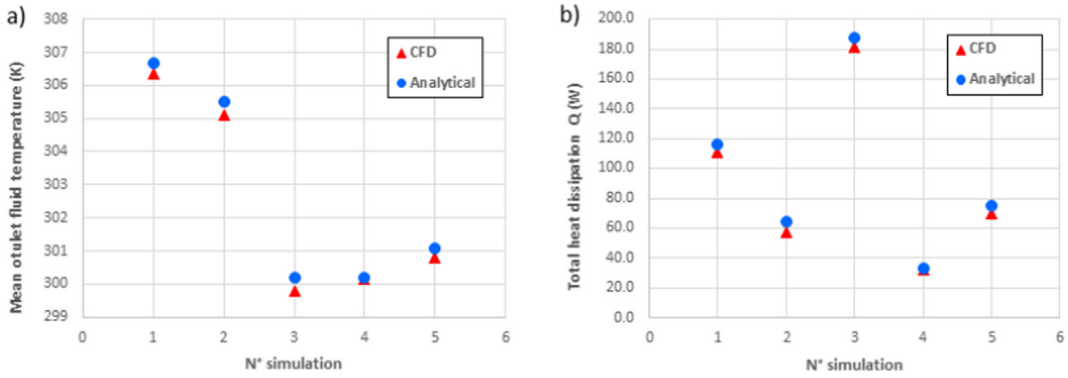

Fig. 14. Random simulations: Mean outlet fluid temperature (a), total heat dissipation Q (b).

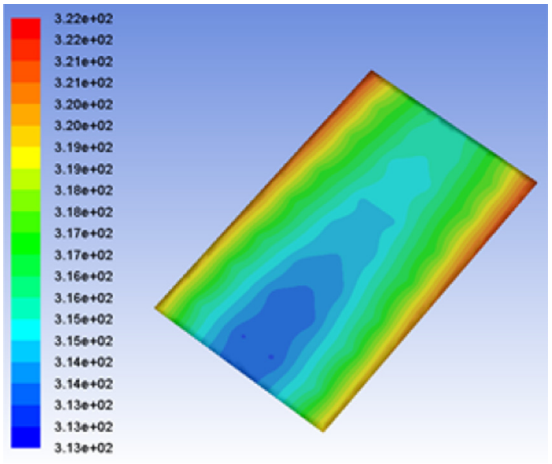

Fig. 15. Top wall temperature variation (K); for $u_0 = 9.1$ m/s, $T_0 = 294.8$ K, $T_w = 350$ K.

$T_0 \in [284.82; 304.82]$ K, $u_0 \in [8.3; 11.0]$ m/s and $T_w \in [300; 420]$ K. The study of the inlet velocity shows that the analytical predictions of the mean outlet fluid temperature are slightly under-estimated compared to the CFD-based results when u_0 is lower than 8.3 m/s. This under-estimation comes from the value of the local heat transfer coefficient. According to the empirical correlation from [27], the local heat transfer coefficient of the lattice varies only with respect to the Reynolds number of the flow, i.e. with respect to the airflow velocity. Therefore, when the inlet airflow velocity u_0 decreases, the local heat transfer coefficient of the lattice $h_{\infty_{lat}}$ decreases, accordingly.

The numerical local heat transfer coefficient determined from the CFD model is compared to the empirical value of $h_{\infty_{lat}}$ used in the analytical model, see Fig. 17.

For $T_0 = 294.8$ K and $T_w = 320$ K, the analytical mean outlet fluid temperature is in good agreement with the CFD predictions when the empirical local heat transfer coefficient is at least 1.5 times greater than the numerical one, i.e. when the inlet airflow velocity is between 8.3 and 11 m/s. The analytical model built with a fin analysis constitutes an approximate solution of the problem, whereas the CFD model involves both Navier-Stokes and energy equations to be solved simultaneously. Besides, the numerical calculation of the surface heat transfer coefficients remains much more complex than the empirical correlation as it does not only depend on the airflow velocity but also on the temperature. Therefore, at flow velocities below 7 m/s, the approximate solution does not seem valid as the mean outlet fluid temperature is underestimated due to values of the empirical and numerical local heat transfer coefficients that are quite close. As a consequence, it is recommended to use the analytical model for the range of airflow velocities [8.3; 11] m/s, where a very good agreement between analytical and CFD solutions is obtained.

4.3. Scope of the model & validation

The analytical model is much faster than the CFD model as the computational demand is much lower for the former. Both mean outlet fluid temperature and total heat dissipation can be instantly determined with the analytical code, whereas the CFD simulation requires a significant longer time, depending on the available computational resources. The analytical model therefore represents a rapid and cost-effective tool to predict the thermal performance

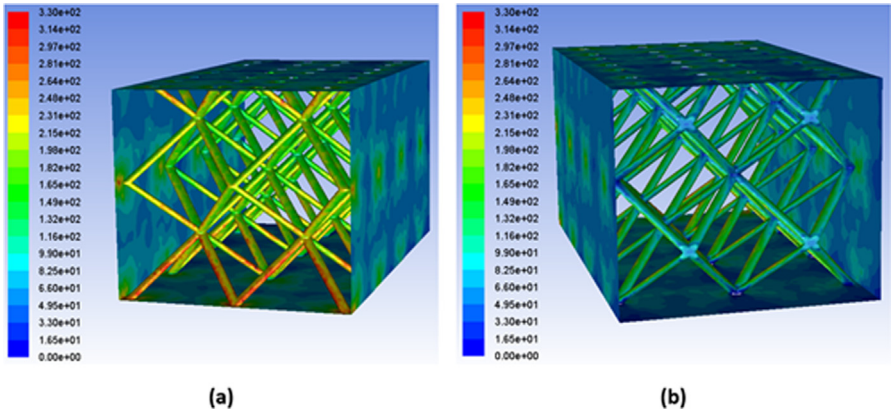

Fig. 16. Local heat transfer coefficient (W/m^2·K): inlet view (a), outlet view (b).

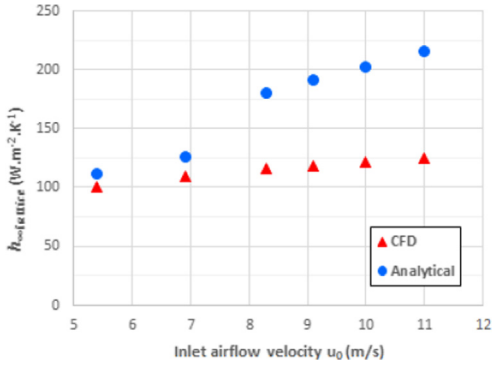

Fig. 17. Variations of the local heat transfer coefficient of lattice with respect to u_0.

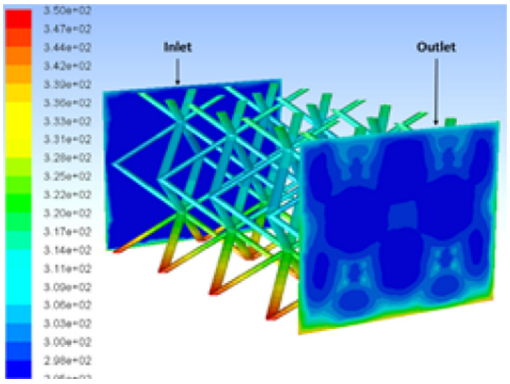

Fig. 19. Fluid temperature distribution (K) at both inlet and outlet.

of the studied multi-layered lattice sample. However, some potential limitations should be brought to attention as the analytical model has been developed for one particular lattice sample with cylindrical struts of diameter $d = 0.002$ m and a unit cell size $a = 0.02$ m. Due to the recent development and enhancement of additive manufacturing, a wide variety of multi-layered lattice samples exhibiting different cylindrical struts diameter and unit cell sizes has been created through 3D-printing, see such examples in Fig. 18.

The discretisation of the studied sample into cells used for calculating the fluid temperature distribution in the analytical model, could be re-utilised for other samples with smaller cell sizes. However, the model is expected to show limitations for very small cell sizes due to the 'no fluid mixing' assumption in the channel. The smaller the cell size, the more significant the fluid mixing between the layers in the vertical direction.

The analytical code might not work well for different types of geometry and materials, this would however require further investigation. Its applicability and validity should be studied for other samples and compared with experimental data. This would allow this model to be fully validated experimentally rather than being only compared to CFD based results. Experiments would need to be performed under the same conditions, i.e. the outer surfaces of the heat sink being thermally insulated, with a heat source applying a constant temperature on the bottom surface of the heat sink, air generated by an external source (fan, pump) being forced to flow through the sample, and measurements performed under steady-state conditions. The experimental set-up detailed in [12] to study forced convection within lattice-frame materials could be reproduced for complex multi-layered lattice samples.

For convenience, several experimental studies [4,29] only considered one thermocouple at the heat sink outlet to measure the mean outlet fluid temperature. However, the post-processing of the temperature performed with Fluent and illustrated in Fig. 19 shows that the fluid temperature variation at the outlet is not negligible. Therefore, the experimental set-up suggested in [26] appears to be more suitable for measurements of the mean outlet fluid temperature as multiple thermocouples are placed at different locations along the sample height direction.

The pressure drop across the sample should also be investigated as it is an important parameter for structural concerns and for the thermal performance of heat sinks. According to [10], the analytical investigation of the pressure drop does not remain practical due to the complexity of the physical problem, therefore, the pressure drop could be numerically investigated through CFD, and through experiments, considering the set-up defined in [26]. Heat sinks geometrical parameters, such as the porosity and the surface area density for instance, have a significant effect on the pressure drop [26]. In addition, the pressure drop from oscillating flow through metal foams has been experimentally studied in [30] and it has been shown that this parameter is highly dependent on the Reynolds number. The higher the flow velocity, the higher the pressure drop across the heat sink.

5. Conclusions

A rapid and cost-effective analytical model able to predict the thermal performance of complex lattice structures has been developed. This model is able to instantly predict both the mean outlet fluid temperature and the total heat dissipated by the structure for given inputs conditions. A very good agreement between analytical and CFD predictions is obtained for both the mean outlet fluid temperature and the total heat dissipation as the average relative errors reach approximately 0.1% and 5.6%, respectively, for the following ranges of inputs: inlet airflow temperature T_0 within $[284.8; 304.8]$ K, inlet airflow velocity u_0 within $[8.3; 11]$ m/s, and heating temperature T_w within $[300; 420]$ K. Further investigation

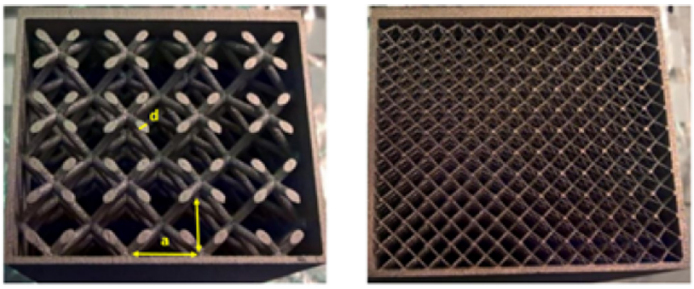

Fig. 18. Other metallic multi-layered lattice samples with body-centered cubic (BCC) cells (photos courtesy of SAFRAN Ltd.).

should however be performed on other multi-layered lattice samples with smaller struts diameter and unit cell sizes to assess the applicability of the analytical approach for a wider range of conditions. Even though the analytical model has been numerically verified with CFD for the studied sample, experiments should be considered for the full validation of the model.

Declaration of Competing Interest

The authors declare that there is no conflict of interest.

Acknowledgments

The authors acknowledge the technical support from SAFRAN Electrical & Power UK LTD. Data underlying this study can be accessed through the Cranfield University repository at https://doi.org/10.17862/cranfield.rd.9873233.

References

[1] H.E. Ahmed, B.H. Salman, A.S. Kherbeet, M.I. Ahmed, Optimization of thermal design of heat sinks: a review, Int. J. Heat Mass Transf. 118 (2018) 129–153.
[2] A. Bouknadel, I. Rah, H. El Omari, H. El Omari, Comparative study of fin geometries for heat sinks in natural convection, in: 2nd International Renewable and Sustainable Energy Conference, IRSEC 2014, Ouarzazate, Morocco, 2014.
[3] S. Zulk, T. Köneke, A. Mertens, Analytical modeling of plate fin heat sinks for natural convection cooling in power electronics, in: 13th IEEE Vehicle Power and Propulsion Conference, VPPC 2016, Zhejiang Hotel Hangzhou, China, 17–20 October, 2016, 2016.
[4] S. Krishnan, D. Hernon, M. Hodes, J. Mullins, A.M. Lyons, Design of complex structured monolithic heat sinks for enhanced air cooling, IEEE Trans. Compon. Packag. Manuf. Technol. (2012) 266–277.
[5] T.J. Lu, Heat transfer efficiency of metal honeycombs, Int. J. Heat Mass Transf. 118 (1999) 2031–2040.
[6] S. Gu, T.J. Lu, A.G. Evans, On the design of two-dimensional cellular metals for combined heat dissipation and structural load capacity, Int. J. Heat Mass Transf. 44 (2001) 2163–2175.
[7] T. Wen, J. Tian, T.J. Lu, D.T. Queheillalt, H.N.G. Wadley, Forced convection in metallic honeycomb structures, Int. J. Heat Mass Transf. 49 (2006) 3313–3324.
[8] S. Liu, Y. Zhang, P. Liu, New analytical model for heat transfer efficiency of metallic honeycomb structures, Int. J. Heat Mass Transf. 51 (2008) 6254–6258.
[9] H. Liu, Q.N. Yu, Z.C. Zhang, Z.G. Qu, C.Z. Wang, Analytical solutions for heat transfer efficiency in metallic honeycombs using two-equation method, Int. Commun. Heat Mass Transf. 75 (2016) 147–153.
[10] M. Bai, J.N. Chung, Analytical and numerical prediction of heat transfer and pressure drop in open-cell metal foams, Int. J. Therm. Sci. 50 (2011) 869–880.
[11] H. Liu, Q.N. Yu, Z.G. Qu, R.Z. Yang, Simulation and analytical validation of forced convection inside open-cell metal foams, Int. J. Therm. Sci. 111 (2017) 234–245.
[12] T. Kim, C.Y. Zhao, T.J. Lu, H.P. Hodson, Convective heat dissipation with lattice-frame materials, Mech. Mater. 36 (2004) 767–780.
[13] Y. Varol, H.F. Oztop, I. Pop, Conjugate heat transfer in porous triangular enclosures with thick bottom wall, Int. J. Numer. Methods Heat Fluid Flow 19 (5) (2009) 650–664.
[14] Y. Varol, H.F. Oztop, I. Pop, Entropy analysis due to conjugate-buoyant flow in a right-angle trapezoidal enclosure filled with a porous medium bounded by a solid vertical wall, Int. J. Therm. Sci. 48 (6) (2009) 1161–1175.
[15] H.F. Oztop, Z. Fu, B. Yu, J. Wei, Conjugate natural convection in air filled tube inserted a square cavity, Int. Commun. Heat Mass Transf. 38 (5) (2011) 590–596.
[16] H.F. Oztop, C. Sun, B. Yu, Conjugate-mixed convection heat transfer in a lid-driven enclosure with thick bottom wall, Int. Commun. Heat Mass Transf. 35 (6) (2008) 779–785.
[17] A.K. Asl, S. Hossainpour, M.M. Rashidi, M.A. Sheremet, Z. Yang, Comprehensive investigation of solid and porous fins influence on natural convection in an inclined rectangular enclosure, Int. J. Heat Mass Transf. 133 (2019) 729–744.
[18] N.S. Bondareva, M.A. Sheremet, Conjugate heat transfer in the PCM-based heat storage system with finned copper profile: application in electronics cooling, Int. J. Heat Mass Transf. 124 (2018) 1275–1284.
[19] N.S. Bondareva, B. Buonomo, O. Manca, M.A. Sheremet, Heat transfer performance of the finned nano-enhanced phase change material system under the inclination influence, Int. J. Heat Mass Transf. 135 (2019) 1063–1072.
[20] H.M. Ali, A. Arshad, Experimental investigation of n-eicosane based circular pin-fin heat sinks for passive cooling of electronic devices, Int. J. Heat Mass Transf. 112 (2017) 649–661.
[21] A. Arshad, H.M. Ali, M. Ali, S. Manzoor, Thermal performance of phase change material (PCM) based pin-finned heat sinks for electronics devices: Effect of pin thickness and PCM volume fraction, Appl. Therm. Eng. 112 (2017) 143–155.
[22] H.M. Ali, A. Arshad, M. Jabbal, P.G. Verdin, Thermal management of electronics devices with PCMs filled pin-fin heat sinks: a comparison, Int. J. Heat Mass Transf. 117 (2018) 1199–1204.
[23] H.M. Ali, M.J. Ashraf, A. Giovannelli, M. Irfan, T.B. Irshad, H.M. Hamid, F. Hassan, A. Arshad, Thermal management of electronics: an experimental analysis of triangular, rectangular and circular pin-fin heat sinks for various PCMs, Int. J. Heat Mass Transf. 123 (2018) 272–284.
[24] A.I. Alsabery, M.A. Sheremet, M. Ghalambaz, A.J. Chamkha, I. Hashim, Fluid-structure interaction in natural convection heat transfer in an oblique cavity with a flexible oscillating fin and partial heating, Appl. Therm. Eng. 145 (2018) 80–97.
[25] A.C. Bourdillon, P.G. Verdin, C.P. Thompson, Numerical simulations of water freezing processes in cavities and cylindrical enclosures, Appl. Therm. Eng. 75 (2015) 839–855.
[26] J.H. Joo, B.S. Kang, K.J. Kang, Experimental studies on friction factor and heat transfer characteristics through wire-woven bulk Kagome structure, Experimental Heat Transfer 22 (2009) 99–116.
[27] A. Zukauskas, Convective heat transfer in cross flow, in: Handbook of Single-Phase Convective Heat Transfer, Wiley Interscience, New York, 1987 (Chapter 6).
[28] ANSYS. Fluent 15.0 User's Guide, 2013.
[29] V.V. Calmidi, R.L. Mahajan, Forced convection in high porosity metal foams, J. Heat Transf. 122 (2000) 557–565.
[30] K.C. Leong, L.W. Jin, Effect of oscillatory frequency on heat transfer in metal foam heat sinks of various pore densities, Int. J. Heat Mass Transf. 49 (3–4) (2006) 671–681.